Critical metal distributions in volcanogenic massive sulphide (VMS) deposits in British Columbia: A progress report

Chen Wei[1], Dorota K. Pietruszka[1], Stephen J. Piercey[1], Wanda Aylward[2], Sebastian Kommescher[2], Emma Scanlan[3], and Daniel Layton-Matthews[3]

[1] Department of Earth Sciences, Memorial University of Newfoundland, 9 Arctic Avenue, St. John's, NL, A1B 1N3
[2] Core Research Equipment and Instrument Training (CREAIT) Network, Memorial University of Newfoundland, 230 Elizabeth Avenue, St. John's, NL, A1C 5S7
[3] Department of Geological Sciences and Geological Engineering, Queen's University, Kingston, ON, K7L 3N6
[a] corresponding author: c.wei@mun.ca

Recommended citation: Wei, C., Pietruszka, D.K., Piercey, S.J., Aylward, W., Kommescher, S., Scanlan, E., and Layton-Matthews, D., 2026. Critical metal distributions in volcanogenic massive sulphide (VMS) deposits in British Columbia: A progress report. In: Geological Fieldwork 2025, British Columbia Ministry of Mining and Critical Minerals, British Columbia Geological Survey Paper 2026-01, pp. 53-67.

Abstract

Quantitative analysis of major and minor elements using electron probe microanalyzer (EPMA) and determination of trace elements using laser ablation-inductively coupled plasma-mass spectrometry (LA-ICP-MS) of samples from the Granduc, Anyox/Hidden Creek, and Goldstream volcanogenic massive sulphide deposits reveal critical metal distributions and elemental partitioning behaviors between various mineral phases. Most of the critical metals, such as Co, are hosted in multiple mineral phases with highly variable concentrations. Cobalt enrichment follows the sequence: $Co_{cobaltite}$>$Co_{willyamite}$>Co_{pyrite}>$Co_{pyrrhotite}$>$Co_{sphalerite}$> $Co_{magnetite}$. LA-ICP-MS imaging shows that individual mineral phases can simultaneously accommodate several critical metals. For the magnetite-pyrrhotite-chalcopyrite assemblage: magnetite is enriched in Mg, Al, V, Mn, and Ga; pyrrhotite preferentially hosts Co and Ni; and chalcopyrite concentrates Zn, Se, In, Ag, and Cd. In addition, trace elements in sphalerite, particularly critical metals Co, Ga, In, and Sn, display remarkable variations across the VMS deposits studied. These differences appear to be mainly controlled by geological setting and ore-forming processes, with limited influence from variations in inferred hydrothermal fluid temperature and sulphur fugacity (fS_2) The next phase of work will include developing quantitative models for critical metal deportment, demonstrating how systematic regularities in the partitioning of specific critical metals among coexisting minerals can be used to predict their mineralogical distribution in VMS systems.

Keywords: Volcanogenic massive sulphide, critical metal abundance, elemental partitioning behavior, electron probe, LA-ICP-MS

1. Introduction

The low-carbon, green energy transition is driving unprecedented demand for critical metals, such as copper (Cu), cobalt (Co), and nickel (Ni), which are vital for technologies such as electric vehicles, batteries, and wind turbines (e.g., Jowitt et al., 2018; Reich and Simon, 2024). Volcanogenic massive sulphide (VMS) deposits are important Canadian and global suppliers of base and precious metals, including Cu, Zn, Pb, Au, and Ag (e.g., Franklin et al., 2005; Galley et al., 2007; Piercey, 2011; Hannington, 2013) and can also be economically significant sources of metals such as Co, Ga, Se, Cd, In, Sn, Sb, Tl, and Bi (e.g., Layton-Matthews et al., 2008; Monecke et al., 2016; Piercey et al., 2025).

The VMS deposits in British Columbia represent an important past and potentially future economic contributor to the provincial mining sector (e.g., Hickin et al., 2024). Recent work has shown that VMS deposits in British Columbia contain a variety of critical metals currently on the national critical minerals list (NRCan, 2024), such as Co, In, Sn, Sb, Te, and Bi (e.g., Piercey et al., 2025; Cawood et al., 2025). Although many of these commodities are present as trace elements within mineral phases, their absolute abundance, distribution, and mineral-scale partitioning are not well resolved.

In-situ microanalytical techniques such as electron probe microanalyzer (EPMA) and laser ablation-inductively coupled plasma-mass spectrometry (LA-ICP-MS) provide micron-scale spatial resolution for mineral chemistry. EPMA has high spatial resolution (down to 1 μm) but is constrained by relatively high detection limits (commonly >100 ppm), limiting its utility for accurately measuring many elements at trace levels (Zhao et al., 2015). In contrast, LA-ICP-MS allows for the simultaneous analysis and characterization of multiple elements within a single mineral grain down to sub-ppm levels (e.g., Sylvester, 2006; Cook et al., 2016; Danyushevsky and Thompson, 2025).

Together, EPMA and LA-ICP-MS provide complementary constraints on mineral chemistry. This paper establishes an integrated analytical approach to evaluate critical element distributions and partitioning between different mineral phases in British Columbia VMS deposits. Here, we summarize progress and present representative examples of quantitative EPMA analysis of major and minor elements and LA-ICP-MS spot and mapping analyses of trace elements in mineral phases

from the Granduc, Anyox/Hidden Creek, and Goldstream mafic-siliciclastic (or Besshi) VMS deposits (Fig. 1). These results are used to: 1) evaluate critical-metal distributions across different mineral assemblages using Co as a case study; 2) investigate elemental partitioning among coexisting, spatially associated minerals; and 3) use sphalerite as an example to evaluate the trace element distributions and the factors controlling their variations. The full results of our analytical work can be found in a supplementary publication (Pietruszka et al., 2026).

2. Samples and mineralogy

Samples used in this study were previously reported by Piercey et al. (2025). These samples were obtained from the archives of the British Columbia Geological Survey and the Mineral Deposit Research Unit at the University of British Columbia. Here, we focus on three mafic-siliciclastic VMS deposits: Goldstream (n=2), Anyox (Hidden Creek) (n=3), and Granduc (n=4). Past producers and resources of Cu, these deposits contain byproduct critical metals, including Co (e.g., Peter and Scott, 1999).

The samples were analyzed by bulk assays (see Piercey et al., 2025 for details), and most were subjected to detailed mineral chemical investigations. The main ore and gangue mineral assemblages for the studied samples in these three deposits are summarized in Table 1. Overall, the three deposits share broadly similar major mineral phases, but differ in their minor and trace mineral phases. Specifically, the mineral assemblage from the Anyox (Hidden Creek) deposit consists of pyrite, pyrrhotite, chalcopyrite, and minor sphalerite and hematite (Table 1; Figs. 2a-b). Associated gangue minerals are amphibole, chlorite, quartz, plagioclase, and calcite, and minor apatite and dolomite. The predominant sulphide phases in the Goldstream deposit are pyrrhotite, chalcopyrite, and minor sphalerite, with minor galena (Table 1; Figs. 2e-f). The gangue minerals include amphibole, chlorite, quartz, calcite, muscovite, biotite, and minor plagioclase and apatite. The Granduc deposit has a more complex mineral assemblage, including magnetite, pyrite, pyrrhotite, chalcopyrite, and minor sphalerite, galena, cobaltite, and willyamite, with trace molybdenite (Table 1; Figs. 2c-d). The gangue minerals are predominantly amphibole, chlorite, quartz, calcite, epidote, muscovite, apatite, and minor dolomite.

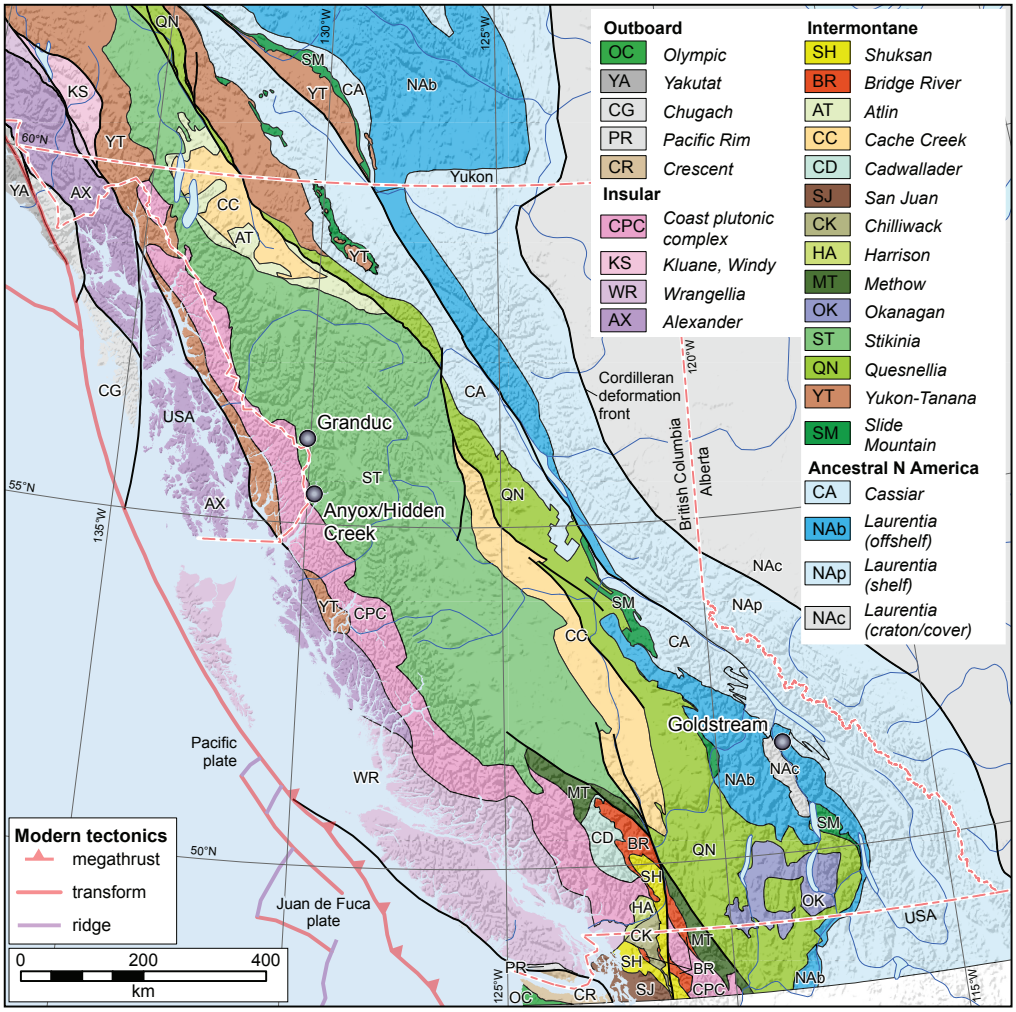

Fig. 1. Location of volcanogenic massive sulphide deposits sampled for this study. Terrane boundaries after Colpron (2020).

Table 1. Summary of mineral phases identified in selected samples from the Granduc, Anyox/Hidden Creek, and Goldstream deposits.

Deposits	Sample ID	Oxides			Sulphides								Main gangue mineral association												Accessory minerals
		Mt	Hem	Ilm	Cob	Wly	Py	Po	Ccp	Sph	Mo	Gn	Px	Chl	Qz	Am	Cal	Ep	Sd	Msc	Bt	Ap	Dol	Pl	Ilt	
Anyox	An-1		xx				xxx	xxx	xxx	xx				xx	x	xxx	xxx					x	x			Talc, Tit, Mrc
	Anyox-1-1						xxx	xx	xx	x				x	xxx		xxx	x		x				xx		Tit, Grh
	Anyox-2						xxx	xxx	xxx	x		x		x		x	xxx					x	x			
Goldstream	HW-2v						x	xxx	xxx	x			x	xxx	xxx	x	xxx	x		xxx	xxx	xxx		xx	xx	Tit, Rut, All
	TS2302						x	xxx	xxx	xxx		x	x	xx	xxx	x	xxx	x	x	xxx	x	x			x	Tit, All
Granduc	GD-9	xxx			x	x		xxx	xxx	x	x	x	xx	xx	xxx	xxx	xxx	xxx	x	xx		xx				Tit, All
	GD-9-02	xxx			x	x		xxx	xxx	x	x	x	x	xxx	xxx	xxx	xxx	xxx	x	x			x			Tit, All
	GR01-112	xxx		x			xxx	xxx	xxx	xx			xx	xxx	xxx	xxx	xxx	xx		xxx		xxx	x			Tit, All
	GRANDUC	xxx			x		x		xxx	xx	x		x	x	x	xxx	x		x	x		xx				

Note: Mineral phases were identified using MLA and verified by SEM and optical microscopy. The Fe-oxides and sulphides are considered reliable, and all major phases are included. Some gangue minerals, particularly silicates, may be present but were not accurately quantified.

x=trace (<1 wt.%); xx=minor (1-5 wt.%); xxx=major (>5 wt.%). Mineral abbreviations: All-allanite; Am-Amphibole; Ap-Apatite; Bt-Biotite; Cal-Calcite; Ccp-Chalcopyrite; Chl-Chlorite; Cth-Clausthalite; Cob-Cobaltite; Dol-Dolomite; Ep-Epidote; Gn-Galena; Graphite-Grh; Hem-Hematite; Ilt-Illite; Ilm-Ilmenite; Marcasite-Mrc; Mt-Magnetite; Mo-Molybdenite; Msc-Muscovite; Pl-Plagioclase; Py-Pyrite; Px-Pyroxene; Po-Pyrrhotite; Qtz-Quartz; Rut-Rutile; Sd-Siderite; Sp-Sphalerite; Tit-Titanite; Wly-Willyamite.

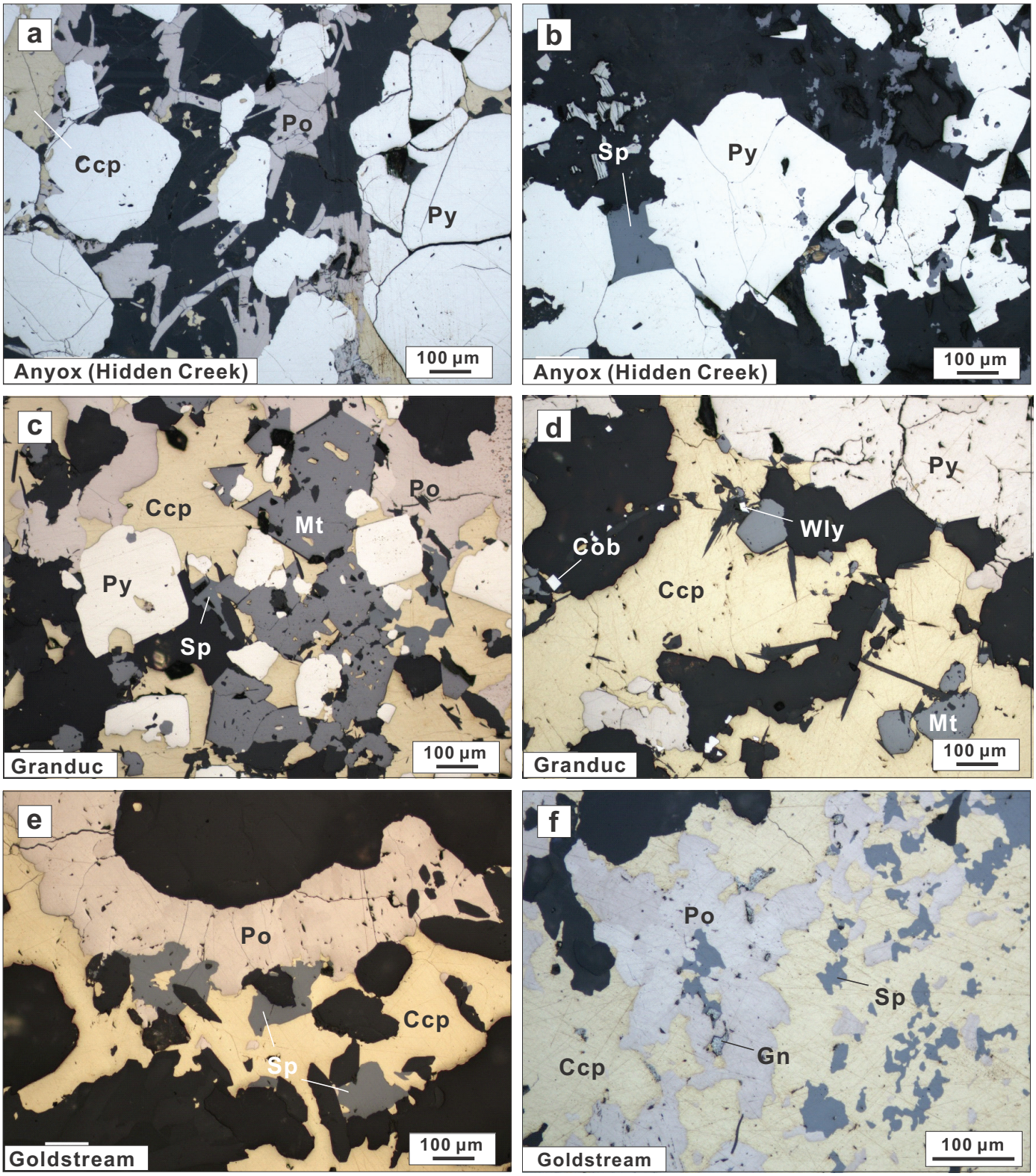

Fig. 2. Reflected light photomicrographs of samples from the Anyox/Hidden Creek, Granduc, and Goldstream deposits. **a)** Pyrrhotite and chalcopyrite along the margins of euhedral pyrite, infilling interstitial voids. **b)** Sphalerite fills vugs within euhedral pyrite crystals. **c)** Euhedral magnetite and pyrite overgrown or enclosed by later-formed chalcopyrite and pyrrhotite. **d)** Fine-grained euhedral willyamite and cobaltite in vugs of chalcopyrite. **e)** Typical association of pyrrhotite, chalcopyrite, and sphalerite. **f)** Pyrrhotite partially replaced by chalcopyrite, which also hosts minor interstitial sphalerite. Abbreviations: Ccp-Chalcopyrite; Cob-Cobaltite; Gn-Galena; Mt-Magnetite; Py-Pyrite; Po-Pyrrhotite; Sp-Sphalerite; Wly-Willyamite.

Given that ore minerals likely host most of the critical elements, we analyzed sulphide minerals, including pyrite, pyrrhotite, chalcopyrite, sphalerite, locally cobaltite, and willyamite, together with coexisting Fe-oxides such as magnetite, across different mineral assemblages (Pietruszka et al., 2026).

3. Analytical methods

Mineral chemistry of these mineral phases was quantified by EPMA and LA-ICP-MS. EPMA was used for phase identification and to provide major- and minor-element data. LA-ICP-MS mapping was used to evaluate grain-scale spatial variability and to constrain elemental partitioning among coexisting phases, whereas LA-ICP-MS spot analyses were used to quantify trace-element concentrations.

3.1. Electron probe microanalysis

The chemical compositions of sulphides and Fe-oxides were determined at the Hibernia Electron Beam Facility at the Core Research Equipment and Instrument Training (CREAIT) Network in the Department of Earth Sciences, Memorial University of Newfoundland. We used a JEOL JXA-8230 SuperProbe EPMA equipped with five wavelength-dispersive spectrometers (WDS) and a tungsten filament electron gun. The analyses were performed using an accelerating voltage of 20 kV, a 20-nA beam current, and the beam focused to 1 µm. Elemental counting times ranged from 5 to 30 s, including 5 to 15 s for background measurements and 10 to 30 s on peak signals for calibration. The full list of analyzed elements for each mineral, together with primary and interference standards, is provided in Pietruszka et al. (2026). Both natural and synthetic standards were used to calibrate the instrument. Additional secondary standards were measured periodically (i.e., for each mineral phase at the start of each run, after 20-25 unknown analyses, and at the end of each run) to demonstrate their reproducibility. Sulphide analyses with totals falling outside the 100 ±2 wt.% range were rejected.

3.2. LA-ICP-MS elemental imaging

LA-ICP-MS elemental maps were carried out by an ESI-NWR 193 nm ArF Eximer laser ablation system coupled with iCAP TQs ICP-MS (Thermo Scientific) at the Queen's Facility for Isotope Research, Queen's University. Element compositional maps were constructed by scanning the target area with a series of parallel laser lines. The ablation was performed at a fluence of 3 J/cm^2 with a constant pulse frequency of 10 Hz. The laser operated with a beam diameter ranging from 5 to 10 µm and a scan speed between 2.5 and 5 µm/s. At the beginning of each raster, a 5-second background measurement was recorded, and a 30-second delay was applied after each line to allow for cell wash-out.

The following isotopes were monitored: ^{23}Na, ^{24}Mg, ^{27}Al, ^{29}Si, ^{32}S, ^{44}Ca, ^{47}Ti, ^{51}V, ^{52}Cr, ^{55}Mn, ^{57}Fe, ^{59}Co, ^{60}Ni, ^{65}Cu, ^{66}Zn, ^{69}Ga, ^{71}Ga, ^{72}Ge, ^{74}Ge, ^{75}As, ^{77}Se, ^{90}Zr, ^{93}Nb, ^{95}Mo, ^{107}Ag, ^{109}Ag, ^{111}Cd, ^{113}In, ^{115}In, ^{118}Sn, ^{121}Sb, ^{125}Te, ^{133}Cs, ^{137}Ba, ^{157}Gd, ^{178}Hf, ^{181}Ta, ^{182}W, ^{185}Re, ^{197}Au, ^{202}Hg, ^{205}Tl, ^{206}Pb, ^{207}Pb, ^{208}Pb, ^{209}Bi, ^{232}Th, and ^{238}U. Two isotopes each for Ag, Ga, Ge, and In were included in the element suite to monitor potential interferences. Rasters were done on reference materials STDGL3 (Belousov et al., 2023), MASS-1 (Wilson et al., 2002), and GSE-1G (Jochum et al., 2005) at the start and end of a mapping run to correct for instrumental drift. Images were compiled and processed using Iolite 4 (Paton et al., 2011). Unlike the quantitative data, element maps cannot be corrected for potential interference for Ga, Ge, and In isotopes. All LA-ICP-MS maps were produced for each element using the same logarithmic colour scale.

3.3. LA-ICP-MS spot analysis

Spot analysis of minor and trace elements in sulphides was performed by LA-ICP-MS using a GeoLasPro 193 nm ArF Excimer laser ablation system (Coherent) coupled to an Element XR HR-ICP-MS instrument (Thermo Scientific) at the Microanalysis Facility at the Core Research and Equipment Training (CREAIT) Network, Memorial University of Newfoundland. Laser ablation was carried out in a pure He atmosphere, with the aerosol mixed with Ar before entering the ICP torch. Spot ablation was carried out using a 30 µm spot size, with an energy density of 5 J/cm^2 and a pulse frequency of 5 Hz. Each analysis consisted of 30 s background acquisition, followed by 40 s ablation, and 30 s washout. Washout time was increased after, for example, high-Pb abundance phases such as galena were analyzed. The ICP-MS was tuned for high sensitivity while maintaining a ThO/Th ratio of $<0.3\%$; all analyses were performed in low-resolution mode. The following isotopes were monitored: ^{24}Mg, ^{27}Al, ^{29}Si, ^{34}S, ^{43}Ca, ^{49}Ti, ^{232}Th, and ^{238}U (dwell time 5 ms); ^{51}V, ^{53}Cr, ^{90}Zr, ^{93}Nb, ^{157}Gd, ^{178}Hf, and ^{181}Ta (dwell time 10 ms); ^{55}Mn, ^{57}Fe, ^{59}Co, ^{60}Ni, ^{65}Cu, ^{66}Zn, ^{69}Ga,^{71}Ga, ^{72}Ge, ^{74}Ge, ^{75}As, ^{77}Se, ^{95}Mo,^{107}Ag, ^{109}Ag, ^{111}Cd, ^{113}In,^{115}In, ^{118}Sn, ^{121}Sb, ^{125}Te, ^{182}W, ^{185}Re, ^{197}Au, ^{202}Hg, ^{205}Tl, ^{206}Pb, ^{207}Pb, ^{208}Pb, and ^{209}Bi (dwell time 20 ms). Reference materials MASS-1 (Wilson et al., 2002) and NIST SRM 610 (Jochum et al., 2011) were used for external calibration. MASS-1 was used for chalcophile and siderophile elements, and NIST SRM610 for lithophile elements. Duplicate analyses of both reference materials were performed at the start of the session and after every 10 to 16 sample analyses to monitor instrument stability and data quality.

Data reduction was done using the LADR software package (Norris and Danyushevsky, 2018). Quantification in both instances was performed using ^{57}Fe as the internal standard for Fe-bearing sulphides including pyrite, pyrrhotite, chalcopyrite, sphalerite, tennantite-tetrahedrite, with all concentrations normalized to 100 wt.%. Significant elemental fractionations relative to Fe were corrected following the method of Danyushevsky et al. (2011). The contents of S and O were estimated based on mono-sulphide and oxide stoichiometry. Isobaric interferences of ^{74}Se on ^{74}Ge, ^{113}Cd on ^{113}In, and ^{115}Sn on ^{115}In were corrected using known isotopic proportions of Cd, Sn, and Se. Interferences of ZrO and NbO on Ag were found to be insignificant due to the low contents of Zr and Nb in the samples.

4. Results

Below, we summarize representative mineral compositions and trace-element distributions among coexisting phases. We first present EPMA data using Co as an example, then present a representative LA-ICP-MS map that illustrates element partitioning, and finally show LA-ICP-MS sphalerite chemistry across the three deposits.

4.1. EPMA mineral compositions

Cobalt concentrations determined by EPMA are reported here for minerals in which Co is detectable. Concentrations vary widely among different minerals, ranging from per cent levels in discrete Co-bearing phases to ppm levels in common sulphides and Fe-oxides (Table 2). Common sulphides such as pyrite, pyrrhotite, sphalerite, and chalcopyrite within the VMS deposits contain minor to trace Co (Fig. 3). In addition to these sulphides, discrete Co-bearing minerals, including cobaltite and willyamite, have been identified in the Granduc deposit (Fig. 2d). Magnetite also hosts trace amounts of Co. Cobaltite and willyamite have the highest Co concentrations, with cobaltite containing 16.9-32.8 wt.% (mean $\pm 2\sigma$: 27.6 ±7.8 wt.%) and willyamite ranging from 14.9-25.5 wt.% (22.7 ±6.0 wt.%). The higher average Co content in cobaltite compared to willyamite indicates a $Co_{Cobaltite} > Co_{willyamite}$ enrichment trend among discrete Co-bearing minerals.

For common sulphide phases, comparisons of Co among these phases are made using the geometric mean, which better represents the central tendency for skewed (≈log-normal) data than the arithmetic mean, given the high variability of Co within individual phases (cf., Wei et al., 2024). Among the major sulphide phases, pyrite is the most Co-rich mineral where present, with the concentrations reaching up to 2.26 wt.% (Table 2). The second Co-rich mineral is pyrrhotite (Fig. 3), which typically contains Co in the range of <0.01 to 0.23 wt.% (Table 2). In sphalerite, more than two-thirds of the analytical spots for all studied deposits are above the detection limits, with the concentrations from <0.01 to 0.14 wt.% (Table 2). Cobalt was only detected in about half (or fewer) of the chalcopyrite analytical spots. Where present, concentrations are generally lower than in sphalerite for Granduc and Goldstream, ranging from <0.01 to 0.05 wt.%. Surprisingly, a spot in chalcopyrite from Granduc has up to 1.56 wt.% Co (Table 2). In addition, magnetite from Granduc generally contains detectable Co, with concentrations from <0.01 to 0.11 wt.% (Table 2).

4.2. LA-ICP-MS elemental mapping

LA-ICP-MS mapping of a magnetite-pyrrhotite-chalcopyrite assemblage from Granduc reveals distinct mineral preferences for certain trace elements (Fig. 4). Magnesium, Al, V, Mn, and Ga are concentrated in magnetite, whereas Co and Ni, and Se are mainly enriched in pyrrhotite. Zinc, Ag, In, Se, and possibly Cd and Te are preferentially enriched in chalcopyrite. Chalcopyrite contains trace amounts of Co and Ni, although their concentrations are lower than those observed in pyrrhotite. The distributions of trace elements such as Mg, Al, Ni, Zn, and possibly Co within the individual mineral phase show considerable heterogeneity. In chalcopyrite, speckled textures marked by patchy enrichment of Co, Ni, and Zn are observed. In magnetite, intersecting stripe-like fabrics enriched in Mg and Al are also present. In addition, grain boundaries of these minerals (possibly galena) show low levels of Sb and Pb.

4.3. LA-ICP-MS trace-element chemistry

In sphalerite, LA-ICP-MS ablation profiles were generally flat and smooth (Fig. 5), suggesting internally consistent concentrations within individual spots; however, element concentrations show considerable variation across spots (Table 3; Fig. 6). The full dataset of minor and trace elements of sphalerite is summarized in Table 3 and can be found in Pietruszka et al. (2026).

Iron is the most common lattice-bound element in sphalerite, typically ranging from 8-12 wt.%. Manganese, Cu, and Cd are also incorporated into the sphalerite lattice, generally at hundreds to tens of thousands of ppm. Trace elements, including Co, Se, Ag, and In, are commonly present at tens to hundreds of ppm. Most of these elements are not unexpected because they are interpreted to substitute for Zn in the sphalerite lattice, either directly or through coupled substitution (e.g., Cook et al., 2009; Ye et al., 2011). Trace elements such as Sn, Sb, and Te occur at around or below 10 ppm, but are detected in more than two-thirds of the analyses. In addition, As, Ge, Ni, Tl, and Bi were predominantly at or below detection limits (Pietruszka et al., 2026).

From a comparison of the three deposits, sphalerite from Anyox is systematically enriched in most trace elements, including Cu (186-9542 ppm; mean=1534 ppm), Ga (9.15-37.4 ppm; mean=17.0 ppm), Ag (7.95-77.5 ppm; mean=23.7 ppm), Cd (3799-5473 ppm; mean=4516 ppm), In (85.8-251 ppm; mean=140 ppm), and Sn (0.79-14.7 ppm; mean=3.39 ppm). In contrast, Goldstream sphalerite has the highest Mn (5839-9957 ppm; mean=7901 ppm) and Te (0.04-6.36 ppm; mean=0.39 ppm), whereas Granduc sphalerite contains the greatest Fe (8.29-17.6 wt.%; mean=10.5 wt.%) and Co (500-1074 ppm; mean=839 ppm). Goldstream sphalerite also exhibits the lowest Cu (17.9-1987 ppm; mean=224 ppm), Ag (0.97-12.8 ppm; mean=4.59 ppm), In (0.33-1.05 ppm; mean=0.57 ppm), and possibly Cd (2453-3879 ppm; mean=3048 ppm). In comparison, Granduc sphalerite exhibits the lowest Ga (<0.07-0.43 ppm) and Sn (<0.21-1.19 ppm), whereas all spots for Co in Anyox sphalerite are below detection limits. In addition, Se concentrations are broadly similar in Goldstream and Granduc sphalerite, whereas Anyox shows a wider range but a lower mean Se content (Fig. 6).

5. Interpretations and discussion

Below, we examine the critical metal distributions among different mineral phases, consider element partitioning among coexisting phases, and evaluate the controls on trace-element variations.

Table 2. Summary of cobalt concentrations in mineral phases determined by EPMA from the Granduc, Anyox/Hidden Creek, and Goldstream deposits.

Deposits	Samples	Statistical Parameter	Cobaltite	Willyamite	Magnetite	Pyrite	Pyrrhotite	Chalcopyrite	Sphalerite
Anyox/Hidden Creek (n = 3)	AN-1	m				15	12	16	9
		% of #DL				47%	92%	63%	67%
		Max				0.06	0.07	0.05	0.05
		Median				0.01	0.03	0.02	0.02
		Mean				0.02	0.03	0.02	0.02
		Min				<0.01	<0.01	<0.01	<0.01
	ANYOX-2	m				11	9	8	
		% of #DL				100%	89%	38%	
		Max				0.45	0.10	0.05	
		Median				0.23	0.04	0.01	
		Mean				0.18	0.04	0.02	
		Min				0.03	<0.01	<0.01	
	ANYOX-1-1	m				19	3	13	5
		% of #DL				42%	67%	62%	0%
		Max				0.04	0.03	0.05	<0.01
		Median				0.01	0.01	0.02	
		Mean				0.02	0.02	0.02	
		Min				<0.01	<0.01	<0.01	
Goldstream (n=2)	HW-2v	m					12	9	1
		% of #DL					92%	44%	0%
		Max					0.08	0.05	<0.01
		Median					0.05	0.01	
		Mean					0.04	0.02	
		Min					<0.01	<0.01	
	TS2303-02	m					6	13	8
		% of #DL					50%	38%	75%
		Max					0.06	0.03	0.05
		Median					0.02	0.01	0.02
		Mean					0.02	0.01	0.02
		Min					<0.01	<0.01	<0.01
Granduc (n= 4)	GR01-112	m	1		23	9	10	18	11
		% of #DL	100%		91%	82%	100%	56%	100%
		Max	16.9		0.11	2.26	0.23	0.05	0.14
		Median			0.05	0.86	0.19	0.02	0.10
		Mean			0.05	0.67	0.19	0.02	0.10
		Min			<0.01	0.16	0.14	<0.01	0.05
	Granduc	m	21		9	2	8	14	3
		% of #DL	100%		78%	100%	100%	36%	100%
		Max	30.0		0.06	0.17	0.16	1.56	0.10
		Median	27.7		0.02	0.13	0.13	0.01	0.08
		Mean	26.4		0.03	0.13	0.12	0.02	0.07
		Min	18.8		<0.01	0.10	0.09	<0.01	0.04
	GD-09	m	12	15	12		7	8	
		% of #DL	100%	100%	67%		100%	50%	
		Max	32.8	25.5	0.05		0.22	0.05	
		Median	31.2	24.2	0.03		0.17	0.02	
		Mean	31.0	22.7	0.03		0.17	0.02	
		Min	29.0	14.9	<0.01		0.14	<0.01	
	GD-09-2	m			20			8	
		% of #DL			100%			63%	
		Max			0.10			0.05	
		Median			0.07			0.03	
		Mean			0.06			0.02	
		Min			0.01			<0.01	

n, the numbers of analyzed samples. Mean, geometric mean; m, the number of measurements; % of #DL**,** the percentage of analyzed values above the detection limit. If <50% of data were below the detection limit, those values were set to the detection limit for the calculations of the medians and means (cf., van den Boogaart and Tolosana-Delgado, 2013).

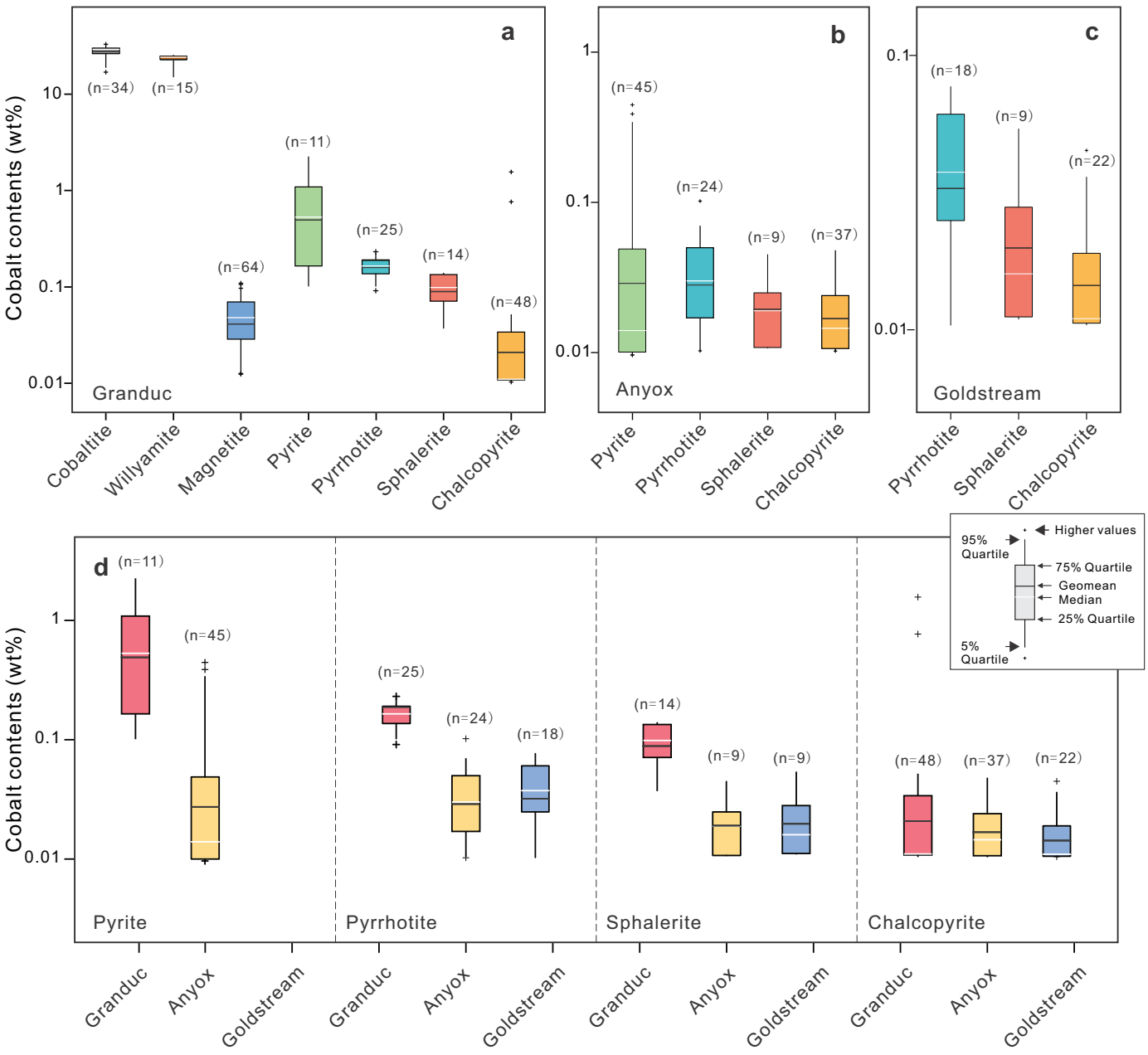

Fig. 3. Box-and-whisker plots displaying Co concentrations in different mineral phases. **a)** Granduc deposit. **b)** Anyox/Hidden Creek deposit. **c)** Goldstream deposit. **d)** Co concentrations in common sulphide minerals across all three deposits. Data below the detection limits are replaced by their detection limits included in the plots.

5.1. Critical-metal distribution among mineral phases

Bulk rock assays demonstrated that mafic-siliciclastic VMS deposits in British Columbia contain higher levels of Co, Cu, In, Mn, Se, Sn, and Te relative to felsic-hosted deposits (Piercey et al., 2025). However, the specific minerals bearing these critical metals remain unclear because most are present only as minor or trace components within mineral phases (Piercey et al., 2025), except for the primary commodities of Cu and Zn. We use the distribution of Co as an illustrative example.

Cobalt concentrations determined by EPMA are used here for comparison because Co in the most Co-bearing minerals previously recognized is well above the EPMA detection limits (Table 2) and the fine grain size of some Co-bearing minerals precludes reliable LA-ICP-MS spot analyses due to signal mixing with adjacent phases. Overall, for each mineral phase, Co concentrations vary significantly among the three deposits (Fig. 3). This deposit-level pattern is similar across all analyzed sulphides: Granduc has the highest Co concentrations in pyrite, pyrrhotite, and sphalerite, followed by Goldstream and Anyox. In chalcopyrite, however, Co concentrations do not show the same systematic difference between Goldstream and Anyox (Fig. 3d).

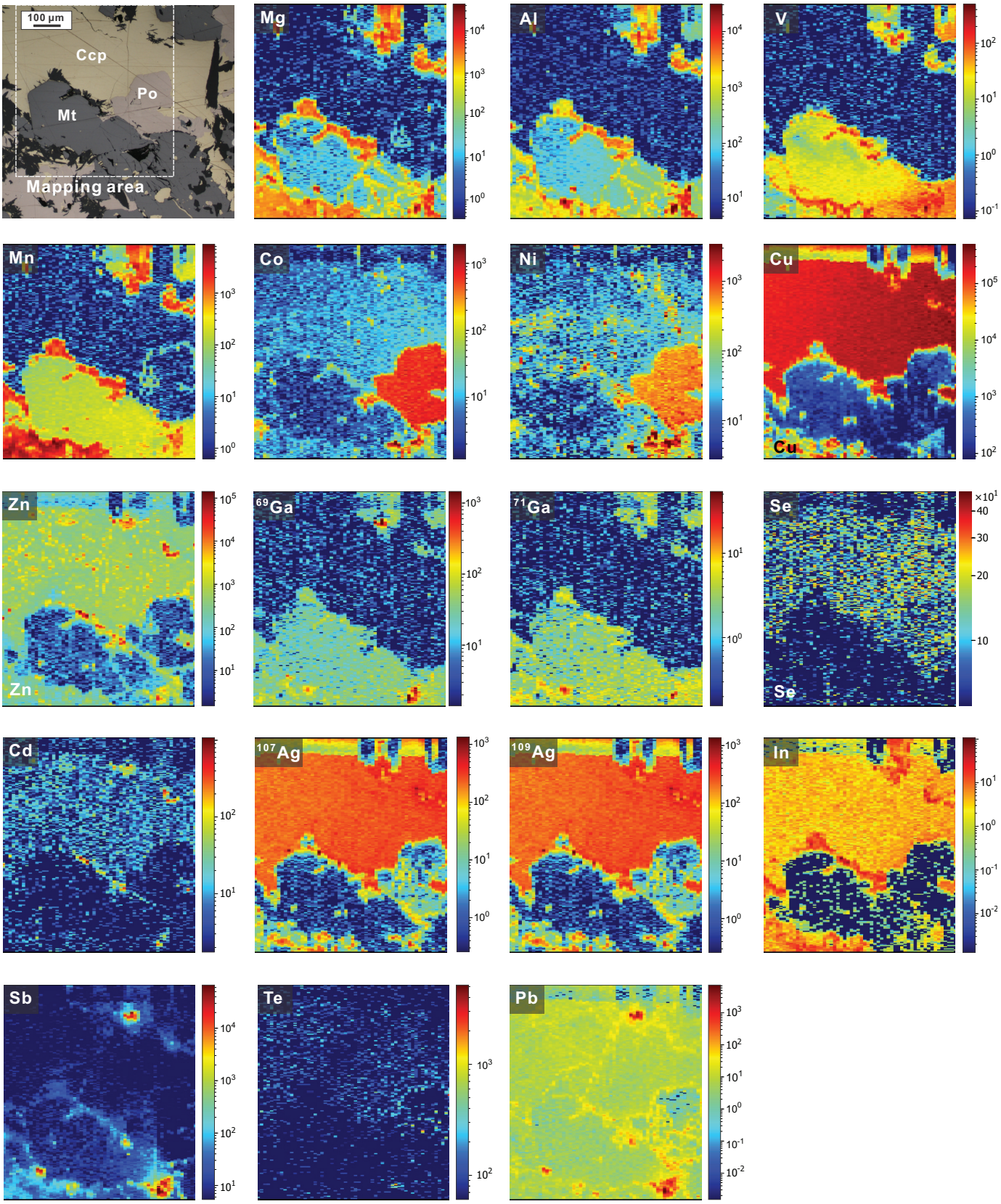

Fig. 4. LA-ICP-MS element maps of the magnetite-pyrrhotite-chalcopyrite assemblage; top left is a reflected light image. Elemental maps illustrate mineral-specific enrichment and partitioning among magnetite, pyrrhotite, and chalcopyrite. Scales in counts-per-second (cps). Sample from the Granduc deposit.

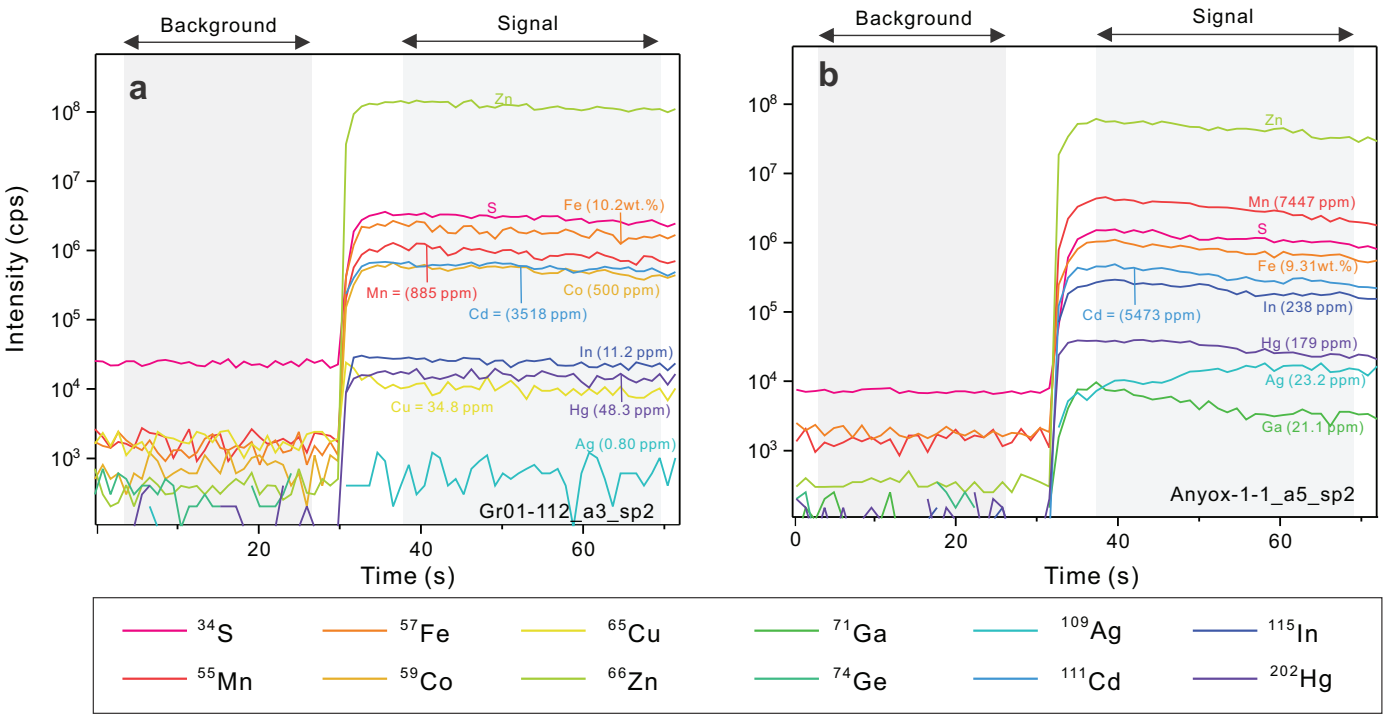

Fig. 5. Typical single-spot LA-ICP-MS spectra for selected elements in sphalerite. **a)** Time-resolved depth profile of Co-rich sphalerite from Granduc deposit. **b)** Smooth signals for all elements in In-rich sphalerite from Anyox/Hidden Creek deposit. Numbers in brackets are concentrations.

Despite these inter-deposit differences in absolute Co concentrations, the relative enrichment sequence among mineral phases is consistent across the studied samples: $Co_{cobaltite}$>$Co_{willyamite}$>Co_{pyrite}>$Co_{pyrrhotite}$>$Co_{sphalerite}$>$Co_{magnetite}$. This mineral-specific sequence is also broadly consistent across the different mineral assemblages examined (Fig. 3a), suggesting a consistent mineralogical control on Co partitioning across assemblage types. Similar Co partitioning among pyrite-pyrrhotite-sphalerite-magnetite associations has been reported in other types of deposits, including skarn Fe deposits and magmatic Fe-Ti oxide deposits (e.g., Liang et al., 2023; Zhang et al., 2025). However, Co in chalcopyrite commonly approaches EPMA detection limits, which rules out a quantitative assessment of Co partitioning between magnetite and chalcopyrite based on EPMA spot data alone. We further use LA-ICP-MS mapping in the following section to assess the relative Co enrichment between these two minerals in a textural context.

5.2. Partitioning and enrichment among coexisting phases

Except for Cu and Zn, most critical metals occur in trace levels in host minerals (e.g., Reich and Simon, 2024). The LA-ICP-MS element imaging technique enables visualizing the spatial distribution of elements of interest at scales from µm to cm, providing direct insight into how these metals are distributed and partitioned among various minerals (Chew et al., 2021). To quantify partitioning behaviors of critical metals, we use a sample with magnetite-pyrrhotite-chalcopyrite mineral assemblage to illustrate elemental partitioning behaviors and to evaluate the reliability of identifying Co-host phases through EPMA.

The partitioning of critical metals, such as Co, Ga, Ge, Se, In, Sb, Te, and Bi in base metal sulphides, seems to be relatively well-constrained (George et al., 2016; Xu et al., 2021; Wei et al., 2024; Cawood et al., 2025, and references therein). However, it remains unclear how these elements are partitioned between Fe-oxide and sulphide phases, especially because magnetite can host critical metals such as Co, Ga, and Ge (e.g., Dare et al., 2014; Nadoll et al., 2014; Zhang et al., 2025).

In the Granduc sample, the LA-ICP-MS maps show that the highest levels of Co and Ni are in pyrrhotite, followed by chalcopyrite, and the lowest in magnetite (Fig. 4). This suggests a partitioning trend for both elements: $Co_{pyrrhotite}$> $Co_{chalcopyrite}$>$Co_{magnetite}$ and $Ni_{pyrrhotite}$>$Ni_{chalcopyrite}$>$Ni_{magnetite}$. The pattern is consistent with our EPMA results for the relative enrichment of Co in pyrrhotite over magnetite. Similar trends for Co and Ni have also been reported for the ABM (Yukon) and Windy Craggy (British Columbia) VMS deposits, where pyrrhotite has higher Co and Ni concentrations than chalcopyrite (Denisová et al., 2024; Cawood et al., 2025).

Cobalt partitioning can differ among ore systems and some studies considered that magnetite is enriched in Co relative to chalcopyrite in Fe-skarns (e.g., Liang et al., 2023; Liu et al., 2024). For example, in the Galinge deposits of China, magnetite contains higher Co contents than coexisting chalcopyrite (~7 ppm vs. ~2 ppm; Liu et al., 2024). Such differences likely

Table 3. Summary of sphalerite chemistry as determined by LA-ICP-MS, and estimated crystallization temperatures and $\log_{10}(fS_2)$ values (arithmetic means ±2σ) from the Granduc, Anyox/Hidden Creek, and Goldstream deposits.

Deposits	Sample	Statistical Parameter	Mn (ppm)	Fe (wt.%)	Co (ppm)	Cu (ppm)	Zn (wt.%)	Ga (ppm)	Se (ppm)	Ag (ppm)	Cd (ppm)	In (ppm)	Sn (ppm)	Sb (ppm)	Te (ppm)	$T_{GGIMFis}$ (°C)	$2\sigma_{ext}$ (°C)	$\log_{10}(fS_2)$	$2\sigma_{ext}$ (fS_2)
Anyox (n=2)	An-1 (m=8)	% of #DL	100%	100%	0%	100%	100%	100%	100%	100%	100%	100%	100%	100%	63%				
		Max	4744	10.8	<0.66	9542	57.9	37.4	25.9	77.5	5155	142	12.8	35.3	0.48				
		Median	3834	9.35	-	2144	56.2	10.7	10.4	22.5	4233	111	2.13	10.5	0.13	354 ±8	±76	−8.6 ±0.3	±2.5
		Mean	3822	9.32	-	1707	56.0	14.1	11.7	25.2	4268	109	2.25	10.6	0.16				
		Min	3040	7.77	-	186	53.9	9.15	7.21	7.95	3799	85.8	0.79	3.04	<0.09				
	Anyox-1-1 (m=4)	% of #DL	100%	100%	0%	100%	100%	100%	100%	100%	100%	100%	100%	100%	75%				
		Max	7932	9.74	<0.67	3194	56.3	29.7	272	35.9	5473	251	14.7	17.1	0.74				
		Median	7520	9.40		1051	55.7	24.9	254	20.4	4988	231	8.03	13.2	0.49	354 ±7	±76	−8.6 ±0.3	±2.5
		Mean	7602	9.35		1238	55.7	24.7	257	21.0	5057	231	7.67	9.70	0.45				
		Min	7447	8.87		709	55.1	20.5	251	13.3	4806	212	3.71	3.14	<0.24				
Goldstream (n=1)	TS2303-02 (m=20)	% of #DL	100%	100%	100%	100%	100%	100%	100%	100%	100%	100%	95%	95%	80%				
		Max	9957	11.2	257	1987	57.6	11.6	126	12.8	3879	1.05	2.03	2.15	6.36				
		Median	7952	10.1	185	251	55.2	6.23	93.6	5.94	3057	0.63	0.61	0.69	0.47	340 ±4	±73	−9.2 ±0.2	±2.4
		Mean	7901	10.0	184	224	55.3	5.87	91.8	4.59	3048	0.57	0.74	0.52	0.39				
		Min	5839	8.13	129	17.9	53.8	2.88	54.2	0.97	2453	0.33	0.38	0.06	<0.08				
Granduc (n=2)	GR01-112 (m=8)	% of #DL	100%	100%	100%	100%	100%	73%	100%	100%	100%	100%	91%	91%	73%				
		Max	885	17.6	1074	29681	57.7	0.24	133	26.7	4611	23.4	1.19	11.8	1.84				
		Median	311	9.84	926	579	56.1	0.15	109	9.84	4117	18.8	0.31	2.46	0.26	374 ±5	±78	−7.9 ±0.2	±2.3
		Mean	342	10.2	857	639	55.1	0.14	111	7.07	4098	16.3	0.33	1.48	0.26				
		Min	183	8.29	500	34.8	44.9	<0.07	97.4	0.80	3217	11.2	<0.21	<0.05	<0.08				
	GRANDUC (m=4)	% of #DL	100%	100%	100%	100%	100%	100%	100%	100%	100%	100%	100%	100%	100%				
		Max	190	12.3	1070	7251	55.4	0.43	95.3	45.2	2610	21.8	0.38	5.79	1.13				
		Median	98.5	11.4	730	3607	53.7	0.17	73.5	21.6	2406	9.86	0.32	0.89	0.15	361 ±5	±77	8.5 ±0.1	±2.6
		Mean	111	11.4	790	3377	53.9	0.19	76.6	21.1	2426	11.9	0.28	1.19	0.20				
		Min	82.7	10.6	684	1720	53.0	0.11	67.2	11.3	2294	9.34	0.15	0.48	0.07				

n, Mean, m, % of #DL and median/mean calculation methods are defined as in Table 2. $T_{GGIMFis}$, and $\log_{10}(fS_2)$ are internal uncertainties only, resulting from compositional variations in sphalerite. External uncertainties shown as $2\sigma_{extl}$ in separate columns contain all sources of error, including the calibration of the GGIMFis geothermometer (Frenzel et al., 2016) and the model for $\log_{10}(fS_2)$ based on sphalerite composition (cf. Frenzel et al., 2016). All uncertainty estimates correspond to ±2 standard errors. For $\log_{10}(fS_2)$, most external uncertainty arises from the uncertainty in the absolute GGIMFis temperature.

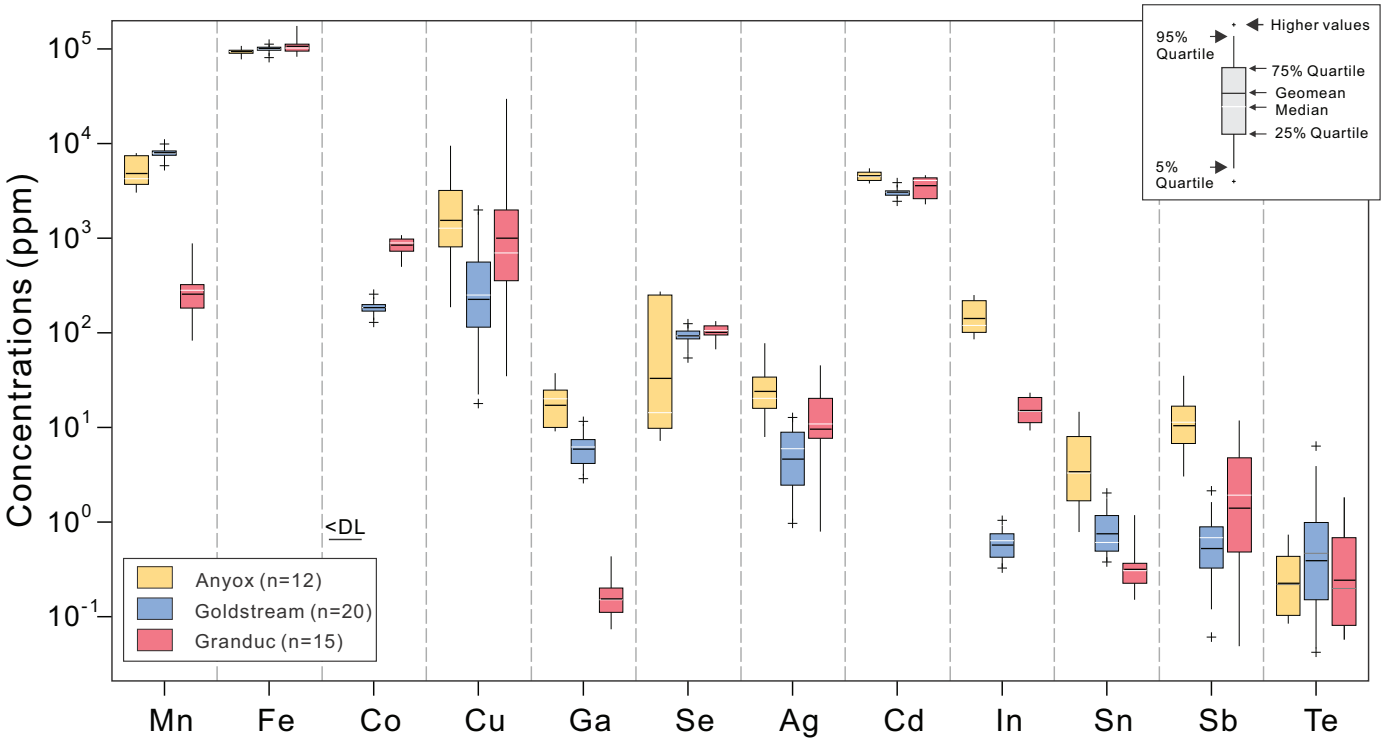

Fig. 6. Box-and-whisker plots of trace element concentrations in sphalerite from the Granduc, Anyox/Hidden Creek, and Goldstream deposits. More than half of the data above detection limits are included in the plots.

reflect variation in ore-forming processes or local geology. In our Granduc samples, LA-ICP-MS spot data indicate low Co concentrations in chalcopyrite (mean ±2δ: 19 ±3 ppm) and in magnetite (less than 10 ppm). Together with the mapping results, these data suggest that chalcopyrite and magnetite are unlikely to be the predominant hosts for Co unless they constitute a large proportion of the ore.

Magnetite also has the highest Ga concentrations in the magnetite-pyrrhotite-chalcopyrite assemblage, exceeding those in pyrrhotite and chalcopyrite (Fig. 4). Detectable Ga in magnetite (20 ppm) has been reported from other VMS deposits (Makvandi et al., 2016). Because Ga is compatible with magnetite via direct substitution into the magnetite lattice ($Ga^{3+} \leftrightarrow Fe^{3+}$; Nadoll et al., 2014), it is readily incorporated into the mineral phase as it precipitates from hydrothermal fluids. If a large amount of magnetite is present in the VMS deposit, it could thus be the main host for Ga.

In addition, chalcopyrite has the highest levels of Zn, Ag, In, Cd, and possibly Te relative to pyrrhotite and magnetite. In our samples, the concentrations of these elements in magnetite are below detection limits, consistent with data from other VMS deposits (Makvandi et al., 2016). Pyrrhotite may contain trace amounts of Zn and Ag, but at levels lower than those determined in chalcopyrite. Thus, for these elements, including Zn, Ag, In, and Cd, their concentrations follow the order: chalcopyrite> pyrrhotite>magnetite. A similar pattern of relative enrichment between chalcopyrite and pyrrhotite was observed for Ag and Zn in the Windy Craggy VMS deposit (Cawood et al., 2025), and for In in the Dulong Sn-Zn(-In) deposit (Xu et al., 2021). Both chalcopyrite and pyrrhotite are enriched in Se, but their relative Se enrichments cannot be determined in this study nor in Cawood et al. (2025). Further investigation is warranted. The lithophile elements such as Mg, Al, V, and Mn are commonly found as minor or trace elements in magnetite (e.g., Dare et al., 2014; Nadoll et al., 2014; Makvandi et al., 2016). Thus, it is not surprising that these elements are preferentially incorporated into magnetite relative to chalcopyrite and pyrrhotite.

5.3. Controls on trace-element variations

In VMS hydrothermal systems, sphalerite is a common sulphide that precipitates across wide physicochemical conditions and accommodates a broad range of minor and trace elements (e.g., Cook et al., 2009; Ye et al., 2011). Consequently, variations in sphalerite trace-element chemistry can record changes in ore-forming conditions (cf., Frenzel et al., 2022; Wei et al., 2025). Here, we use sphalerite as an example to evaluate the controls on trace-element variations. Key factors that may affect the trace element variations in sphalerite include physicochemical conditions (e.g., temperature, pressure, sulphur fugacity [fS_2]), fluid composition, and the competition of other crystallizing mineral phases (e.g., Wei et al., 2021; Frenzel, 2023). To evaluate the effect of temperature and fS_2, we estimated sphalerite crystallization temperatures and fS_2 using the GGIMFis geothermometer and Fe contents in

sphalerite (Table 3; see Frenzel et al., 2016, 2022). Because the temperature and fS_2 ranges overlap among the three deposits within uncertainty, the observed elemental variations appear to show no clear systematic relationship with either temperature or fS_2 change in the current dataset. This suggests that other factors, such as fluid composition and evolution, the source metal endowment, and the competition of co-crystallized mineral phases (cf., Huston et al., 1996), are significant. These potential causes will be evaluated in future work.

Sphalerite is a significant critical mineral host for In, Ga, and Ge in hydrothermal mineral systems (e.g., Frenzel et al., 2017), and the economic recovery of these metals alongside primary commodity Zn has become increasingly important. However, the distribution of these elements varies markedly among deposits and may even vary markedly at the hand-specimen scale. For example, the In and Ga concentrations of sphalerite in the deposits we studied vary by more than three orders of magnitude (Fig. 6; Table 3). It is therefore essential to quantify their concentrations and to resolve their spatial and temporal distributions across deposit-scale and regional-scale frameworks.

In addition to concentration, modal abundance should also be considered. Although chalcopyrite can host minor In, its contents are commonly less than those of co-crystallized sphalerite (e.g., Xu et al., 2021). However, where chalcopyrite is the predominant sulphide in Cu-rich VMS ore and sphalerite occurs only in trace amounts, even very high In concentrations in sphalerite (up to wt.%) may contribute little to the bulk In budget. In such systems, chalcopyrite could be the main In host by virtue of its greater modal abundance. Consequently, assessing the recovery potential of these critical metals must account for both the concentrations of the metals of interest and the modal abundance of their host minerals.

Such mineralogical deportment studies have focused chiefly on precious metals such as Au and Ag (e.g., Chryssoulis and Cabri, 1990; Gregory et al., 2013; Nourizenouz et al., 2025), and PGE (e.g., Cabri et al., 2002; Barnes et al., 2008; Osbahr et al., 2013). However, critical metals have received comparatively little attention (e.g., Frenzel et al., 2019). The next step of our work is to undertake a quantitative mineralogical deportment study to: 1) determine the phase-specific hosts of critical metals in VMS deposits; 2) evaluate how mineral proportions, textures, and liberation characteristics influence mineral deportment and metal distribution; and 3) test if these relationships exhibit predictable regularities across VMS systems. This information is necessary to identify practical options for increasing recoveries and to guide processing strategies in VMS-related mineralization.

6. Summary

The mineral chemistry across various mineral phases from the Granduc, Anyox/Hidden Creek, and Goldstream VMS deposits indicates that critical metals are partitioned among several hosts with markedly different concentrations. For Co, our dataset indicates the following enrichment sequence among analyzed minerals: cobaltite (CoAsS)>willyamite (Co,Ni)SbS >pyrite>pyrrhotite>sphalerite>magnetite. Although not all deposits contain the full suite of these phases, this general trend is broadly consistent across the samples examined. Furthermore, elemental partitioning behavior results show that individual mineral phases can host several different metals of interest. In a magnetite-pyrrhotite-chalcopyrite assemblage, magnetite concentrates Mg, Al, V, Mn, and Ga; pyrrhotite is mainly enriched in Co and Ni; and chalcopyrite preferentially hosts Zn, Ag, Se, In, and Cd. Moreover, trace elements in sphalerite, especially Co, Ga, and In, show considerable variations. This appears to be related to the geological setting of specific deposits and/or ore-forming process rather than variations in temperature and fS_2.

Considering the complex mineral assemblages and multi-host behavior of many critical metals, identifying their mineralogical hosts should consider not only absolute concentrations but also the modal abundance of the host phases. The continued work in this project aims to develop a quantitative model framework for critical metal deportment, demonstrating how systematic regularities in the partitioning of specific critical metals among coexisting minerals can be used to predict their mineralogical distribution in VMS systems.

Acknowledgments

This work was financially and logistically supported by the British Columbia Geological Survey and an NSERC Alliance Missions Critical Minerals grant. Assistance from and discussions with Audrey Graham, Adrian Hickin, Luke Ootes, Alexei Rukhlov, Freia de Waal from the BCGS, and Shaun Barker, Nikola Denisová, and Brian McNulty with MDRU are greatly appreciated. We are also indebted to Colin Aldis at Queen's Facility for Isotope Research for their assistance during LA-ICP-MS elemental imaging. Thanks to Brian McNulty and an anonymous reviewer for constructive comments and suggestions.

References cited

Barnes, S.J., Prichard, H.M., Cox, R.A., Fisher, P.C., and Godel, B., 2008. The location of the chalcophile and siderophile elements in platinum-group element ore deposits (a textural, microbeam and whole rock geochemical study): Implications for the formation of the deposits. Chemical Geology, 248, 295-317.

Belousov, I., Danyushevsky, L., Goemann, K., Gilbert, S., Olin, P., Thompson, J., Lounejeva, E., and Garbe-Schönberg, D., 2023. STDGL3, a reference material for analysis of sulfide minerals by laser ablation ICP-MS: An assessment of matrix effects and the impact of laser wavelengths and pulse widths. Geostandards and Geoanalytical Research, 47, 493-508.

Cabri, L.J., Wilson, J.M.D., Distler, V.V., Kingston, D., Nejedlý, Z., and Sluzheniken, S.F., 2002. Mineralogical distribution of trace platinum-group elements in the disseminated sulphide ores of Noril'sk 1 layered intrusion. Applied Earth Science, 111, 15-22.

Cawood, T.K., Peter, J.M., Petts, D.C., and Polivchuk, M.J., 2025. Syn-and postdepositional controls on the composition of pyrite and pyrrhotite in the Windy Craggy Cu-Co volcanogenic massive sulfide deposit, British Columbia, Canada. Economic Geology, 120.
<https://doi.org/10.5382/econgeo.5181>

Chew, D., Drost, K., Marsh, J.H., and Petrus, J.A., 2021. LA-ICP-MS imaging in the geosciences and its applications to geochronology. Chemical Geology, 559, article 119917. <https://doi.org/10.1016/j.chemgeo.2020.119917>

Chryssoulis, S.L., and Cabri, L.J., 1990. Significance of gold mineralogical balances in mineral processing. Transactions of the Institutions of Mining and Metallurgy. Section C, Mineral processing and extractive metallurgy, 99, C1-C10.

Colpron, M., 2020. Yukon terranes-A digital atlas of terranes for the northern Cordillera. Yukon Geological Survey. <https://data.geology.gov.yk.ca/Compilation/2#InfoTab>

Cook, N.J., Ciobanu, C.L., Pring, A., Skinner, W., Shimizu, M., Danyushevsky, L., Saini-Eidukat, B., and Melcher, F., 2009. Trace and minor elements in sphalerite: A LA-ICP-MS study. Geochimica et Cosmochimica Acta, 73, 4761-4791.

Cook, N., Ciobanu, C.L., George, L., Zhu, Z.Y., Wade, B., and Ehrig, K., 2016. Trace element analysis of minerals in magmatic-hydrothermal ores by laser ablation inductively-coupled plasma mass spectrometry: Approaches and opportunities. Minerals, article 111. <https://doi.org/10.3390/min6040111>

Danyushevsky, L., Robinson, P., Gilbert, S., Norman, M., Large, R., McGoldrick, P., and Shelley, M., 2011. Routine quantitative multi-element analysis of sulphide minerals by laser ablation ICP-MS: Standard development and consideration of matrix effects: Geochemistry: Exploration Environment Analysis, 11, 51-60.

Danyushevsky, L.V., and Thompson, J.M., 2025. Laser Ablation-ICP-MS for the In Situ Analysis of Geological Samples. In: Philip, J.P., Kathryn, L.L., Garbe-Schönberg, D., Philip, R., and Matthew S.A., (Eds.), Horstwood GGR Handbook of Rock and Mineral Analysis. Geostandards and Geoanalytical Research, 49, pp.457-493.

Dare, S.A., Barnes, S.J., Beaudoin, G., Méric, J., Boutroy, E., and Potvin-Doucet, C., 2014. Trace elements in magnetite as petrogenetic indicators. Mineralium Deposita, 49, 785-796.

Denisová, N., Piercey, S.J., and Wälle, M., 2024. Mineralogy and mineral chemistry of the ABM replacement-style volcanogenic massive sulfide deposit, Finlayson Lake district, Yukon, Canada. Mineralium Deposita, 59, 473-503.

Franklin, J.M., Gibson, H.L., Jonasson, I.R., and Galley, A., 2005. Volcanogenic massive sulfide deposits. In: Hedenquist, J.W., Thompson, J.F.H., Goldfarb, R.J., Richards, J.P. (Eds.), Economic Geology 100th Anniversary Volume, pp. 523-560.

Frenzel, M., Hirsch, T., and Gutzmer, J., 2016. Gallium, germanium, indium, and other trace and minor elements in sphalerite as a function of deposit type-A meta-analysis. Ore Geology Reviews, 76, 52-78.

Frenzel, M., Mikolajczak, C., Reuter, M.A., and Gutzmer, J., 2017. Quantifying the relative availability of high-tech by-product metals-the cases of gallium, germanium and indium. Resources Policy, 52, 327-335.

Frenzel, M., Bachmann, K., Carvalho, J.R., Relvas, J.M., Pacheco, N., and Gutzmer, J., 2019. The geometallurgical assessment of by-products-geochemical proxies for the complex mineralogical deportment of indium at Neves-Corvo, Portugal. Mineralium Deposita, 54, 959-982.

Frenzel, M., Voudouris, P., Cook, N.J., Ciobanu, C.L., Gilbert, S., and Wade, B.P., 2022. Evolution of a hydrothermal ore-forming system recorded by sulfide mineral chemistry: a case study from the Plaka Pb-Zn-Ag Deposit, Lavrion, Greece. Mineralium Deposita, 57, 417-438.

Frenzel, M., 2023. Making sense of mineral trace-element data-How to avoid common pitfalls in statistical analysis and interpretation. Ore Geology Reviews, 159, article 105566. <https://doi.org/10.1016/j.oregeorev.2023.105566>

Galley, A., Hannington, M., and Jonasson, I., 2007. Volcanogenic massive sulfide deposits. In: Goodfellow, W.D., (Ed.), Mineral Deposits of Canada: A Synthesis of Major Deposit Types, District Metallogeny, the Evolution of Geological Provinces and Exploration Methods. Geological Association of Canada, Mineral Deposits Division, Special Publication 5, pp. 141-161.

George, L.L., Cook, N.J., and Ciobanu, C.L., 2016. Partitioning of trace elements in co-crystallized sphalerite-galena-chalcopyrite hydrothermal ores. Ore Geology Reviews, 77, 97-116.

Gregory, M.J., Lang, J.R., Gilbert, S. and Hoal, K.O., 2013. Geometallurgy of the Pebble porphyry copper-gold-molybdenum deposit, Alaska: Implications for gold distribution and paragenesis. Economic Geology, 108, 463-482.

Hannington, M.D., 2013. Volcanogenic massive sulfide deposits. In: Holland H.D., and Turekian, K.K., (Eds.), Treatise on Geochemistry, Second Edition. Elsevier, pp. 463-488.

Hickin, A.S., Ootes, L., Orovan, E.A., Brzozowski, M.J., Northcote, B.K., Rukhlov, A.S., and Bain, W.M., 2024. Critical minerals and mineral systems in British Columbia. In: Geological Fieldwork 2005, British Columbia Ministry of Mining and Critical Minerals, British Columbia Geological Survey Paper 2025-01, pp.13-51.

Huston, D.L., Jablonski, W., and Sie, S.H., 1996. The distribution and mineral hosts of silver in eastern Australian volcanogenic massive sulfide deposits. The Canadian Mineralogist, 34, 529-546.

Jochum, K.P., Willbold, M., Raczek, I., Stoll, B., and Herwig, K., 2005. Chemical characterisation of the USGS reference glasses GSA-1G, GSC-1G, GSD-1G, GSE-1G, BCR-2G, BHVO-2G and BIR-1G Using EPMA, ID-TIMS, ID-ICP-MS and LA-ICP-MS. Geostandards and Geoanalytical Research, 29, 285-302.

Jochum, K.P., Weis, U., Stoll, B., Kuzmin, D., Yang, Q., Raczek, I., Jacob, D.E., Stracke, A., Birbaum, K., Frick, D.A., and Günther, D., 2011. Determination of reference values for NIST SRM 610-617 glasses following ISO guidelines. Geostandards and Geoanalytical Research, 35, 397-429.

Jowitt, S.M., Mudd, G.M., Werner, T.T., Weng, Z., Barkoff, D.W., and McCaffrey, D., 2018. The critical metals: An overview and opportunities and concerns for the future. In: Antonio, M.R.A., and Mauk, L.J., (Eds.), Metals, Minerals, and Society. Society of Economic Geologists Special Publication, 21, pp. 25-38. <https://doi.org/10.5382/SP.21.02>

Layton-Matthews, D., Peter, J.M., Scott, S.D., and Leybourne, M.I., 2008. Distribution, mineralogy, and geochemistry of selenium in felsic volcanic-hosted massive sulfide deposits of the Finlayson Lake District, Yukon Territory, Canada. Economic Geology, 103, 61-88. <https://doi.org/10.2113/gsecongeo.103.1.61>

Liang, X., Wang, F.Y., Zhang, L., Zhang, J.W., Wei, C.S., Fan, Y., Guo, X.Z., Zhou, T.F., Zhang, J.Q., and Lü, Q.T., 2023. Cobalt distribution and enrichment in skarn iron deposits: A case study of the Zhuchong skarn iron deposit, Eastern China. Ore Geology Reviews, 163, article 105778. <https://doi.org/10.1016/j.oregeorev.2023.105778>

Liu, T., Jiang, S.Y., Cao, S., Wang, W., Su, H.M., Yang, D., Li, H., and He, S., 2024. Cobalt enrichment and metallogenic mechanism of the Galinge skarn iron deposit in the Eastern Kunlun metallogenic belt, western China. Ore Geology Reviews, 170, article 106147. <https://doi.org/10.1016/j.oregeorev.2024.106147>

Makvandi, S., Ghasemzadeh-Barvarz, M., Beaudoin, G., Grunsky, E.C., McClenaghan, M.B., Duchesne, C., and Boutroy, E., 2016. Partial least squares-discriminant analysis of trace element compositions of magnetite from various VMS deposit subtypes: Application to mineral exploration. Ore Geology Reviews, 78, 388-408.

Monecke, T., Petersen, S., Hannington, M.D., Grant, H., and Samson, I.M., 2016. The minor element endowment of modern sea-floor massive sulfides and comparison with deposits hosted in ancient volcanic successions. In: Verplanck, P.L., and Hitzman, W.M., (Eds.), Rare Earth and Critical Elements in Ore

Deposits. Society of Economic Geologists Special Publication, 18, pp. 115-136. <https://doi.org/10.5382/Rev.18.06>

Nadoll, P., Angerer, T., Mauk, J.L., French, D., and Walshe, J., 2014. The chemistry of hydrothermal magnetite: A review. Ore Geology Reviews, 61, 1-32.

Norris, A., and Danyushevsky, L., 2018, Towards estimating the complete uncertainty budget of quantified results measured by LA-ICP-MS: Goldschmidt conference, 28th, Boston, USA, 2008, Extended Abstracts, p. 1894

Nourizenouz, Z., Guy, B.M., Gutzmer, J., Ebert, D., Braumann, R., and Frenzel, M., 2025. The deportment of silver in Kupferschiefer ores at the Spremberg-Graustein-Schleife deposit, Germany. Mineralium Deposita. <https://doi.org/10.1007/s00126-025-01377-5>

NRCan (Natural Resources Canada), 2024. Critical Minerals List. Government of Canada. <https://www.canada.ca/en/campaign/critical-minerals-in-canada/critical-minerals-an-opportunity-for-canada.html>

Osbahr, I., Klemd, R., Oberthür, T., Brätz, H., and Schouwstra, R., 2013. Platinum-group element distribution in base-metal sulfides of the Merensky Reef from the eastern and western Bushveld Complex, South Africa. Mineralium Deposita, 48, 211-232.

Paton, C., Hellstrom, J., Paul, B., Woodhead, J., and Hergt, J., 2011. Iolite: Freeware for the visualisation and processing of mass spectrometric data. Journal of Analytical Atomic Spectrometry, 26, 2508-2518.

Peter, J.M., and Scott, S.D., 1999. Windy Craggy, northwestern British Columbia; The world's largest Besshi-type deposit. Reviews in Economic Geology, 8, 261-295.

Piercey, S.J., 2011. The setting, style, and role of magmatism in the formation of volcanogenic massive sulfide deposits. Mineralium Deposita, 46, 449-471.

Piercey, S.J., Pietruszka, D., and Goudie, D., 2025. Critical metals in volcanogenic massive sulphide (VMS) deposits in British Columbia: A progress report. In: Geological Fieldwork 2025, British Columbia Ministry of Mining and Critical Minerals, British Columbia Geological Survey Paper 2025-01, pp. 189-201.

Pietruszka, D.K., Wei, C., Piercey, S.J., Aylward, W., and Kommescher, K., 2026. Supplementary data for: Critical metal distributions in volcanogenic massive sulphide (VMS) deposits in British Columbia: A progress report. British Columbia Ministry of Mining and Critical Minerals, British Columbia Geological Survey GeoFile 2026-01, 3 p.

Reich, M., and Simon, A.C., 2024. Critical minerals. Annual Review of Earth and Planetary Sciences, 53, 141-168.

Sylvester, P.J., 2006. Trends in analytical developments and earth science applications in LA-ICP-MS and LA-MC-ICP-MS for 2004 and 2005. Geostandards and Geoanalytical Research, 30(3), 197-207.

Van den Boogaart, K.G., and Tolosana-Delgado, R., 2013. Analyzing compositional data with R: Berlin, Springer, 200 p.

Wei, C., Ye, L., Hu, Y., Huang, Z., Danyushevsky, L., and Wang, H., 2021. LA-ICP-MS analyses of trace elements in base metal sulfides from carbonate-hosted Zn-Pb deposits, South China: A case study of the Maoping deposit. Ore Geology Reviews, 130, article 103945. <https://doi.org/10.1016/j.oregeorev.2020.103945>

Wei, C., Frenzel, M., Ye, L., Huang, Z., and Danyushevsky, L., 2024. Germanium distribution in Mississippi Valley-Type systems from sulfide deposition to oxidative weathering: A perspective from Fule Pb-Zn (-Ge) deposit, South China. American Mineralogist, 109, 1481-1498.

Wei, C., Frenzel, M., Ye, L., de Oliveira, S.B., Danyushevsky, L., Huang, Z.L., and Gutzmer, J., 2025. Sphalerite Chemistry and Carbonate (C, O) Isotope Zonation in the Nayongzhi Mississippi Valley-Type Deposit, Southwest China. Economic Geology, 120, 1751-1776.

Wilson, S.A., Ridley, W.I., and Koenig, A.E., 2002. Development of sulfide calibration standards for the laser ablation inductively-coupled plasma mass spectrometry technique. Journal of Analytical Atomic Spectrometry, 17, 406-409.

Xu, J., Cook, N.J., Ciobanu, C.L., Li, X., Kontonikas-Charos, A., Gilbert, S., and Lv, Y., 2021. Indium distribution in sphalerite from sulfide-oxide-silicate skarn assemblages: A case study of the Dulong Zn-Sn-In deposit, Southwest China. Mineralium Deposita, 56, 307-324.

Ye, L., Cook, N.J., Ciobanu, C.L., Liu, Y.L., Zhang, Q., Liu, T.G., Gao, W., Yang, Y.L., and Danyushevsky, L., 2011. Trace and minor elements in sphalerite from base metal deposits in South China: A LA-ICP-MS study. Ore Geology Reviews, 39, 188-217.

Zhang, Z., Hu, X., Ruan, B., Lv, X., and Liu, R., 2025. Distribution, occurrence and enrichment mechanism of Co in Fe-Ti oxide deposits: An example from the giant Hongge deposit, SW China. Ore Geology Reviews, 177, article 106465. <https://doi.org/10.1016/j.oregeorev.2025.106465>

Zhao, D., Zhang, Y., and Essene, E.J., 2015. Electron probe microanalysis and microscopy: Principles and applications in characterization of mineral inclusions in chromite from diamond deposit. Ore Geology Reviews, 65, 733-748.